Influence of specimen orientation on fatigue crack growth in 7050-T7451 and 2050-T8 aluminium alloys

J.S. Jesus [a,b,*], F.V. Antunes [b], P. Prates [b,c], R. Branco [b], P.V. Antunes [d], L.P. Borrego [b,e], D.M. Neto [b]

[a] Department of Mechanical Engineering, Lisbon Polytechnic - ISEL. Rua Conselheiro Emídio Navarro 1, 1959-007 Lisboa, Portugal
[b] CEMMPRE, Centre for Mechanical Engineering, Materials and Processes, University of Coimbra, Mechanical Engineering Department, Pinhal de Marrocos, 3030-788 Coimbra, Portugal
[c] Department of Mechanical Engineering, Centre for Mechanical Technology and Automation (TEMA), University of Aveiro, 3810-193 Aveiro, Portugal
[d] Escola Superior de Tecnologia de Águeda, TEMA, Universidade de Aveiro, 3810-193 Aveiro, Portugal
[e] Department of Mechanical Engineering, Coimbra Polytechnic - ISEC, Rua Pedro Nunes, Quinta da Nora, 3030-199 Coimbra, Portugal

ABSTRACT

The effect of L-T and S-T orientations on FCGR is here in studied in 7050-T7451 and 2050-T8 aluminum alloys. The Low-cycle fatigue tests and hardness measurements have shown that specimen orientation has a minor effect on material plastic hardening. Lower FCG rates are obtained for both materials in the L-T orientation, which can be associated to the resistance at grain boundaries. The larger cyclic plastic zone attained in the L-T direction leads to an increase of the plasticity inducing crack closure. Crack deflection observed for L-T direction also affects the FCGR due to roughness inducing crack closure, longer crack path and lower effective ΔK.

1. Introduction

Design against fatigue is of major importance in different industrial areas, namely automotive, aerospace, military and aeronautic. The study and understanding of this phenomenon allow to increase the service time of applied materials, as well as improving the safety of structures and machines. Fatigue crack growth (FCGR) in metallic materials depends on the material, geometry and loading of the specimen, component or structure. Material parameters include the crystalline structure of the matrix, material texture, grain size and orientation, size and distribution of precipitates, which may be or not shearable. These features dictate the mechanical behaviour of the materials, namely the material anisotropy.

The effect of specimen orientation, illustrated in Fig. 1 [1], on FCGR was studied by different authors. Leitner *et al.* [2] studied high purity nickel with grain sizes ranging from the micro down to the nanocrystalline regime. They showed that elongated microstructures aligned perpendicular to the crack growth direction can considerably improve the overall resistance against FCG. Grain boundaries serve as preferential crack paths in the entire investigated grain size range. Along with the grain size variation, the influence of the grain aspect ratio was in focus, which can cause a strong orientation dependence of the FCG

behaviour. Leitner *et al.* [3] studied a fully pearlitic steel subjected to severe plastic deformation, which aligned the lamellar structure of the steel parallel to the shear plane. A pronounced anisotropy in the crack propagation behaviour depending on the specimen orientation was observed. The orientation of the crack plane almost parallel to the plate-like lamellae allows the fatigue crack to easily follow the weak crack path along ferrite-cementite interfaces, which resulted in higher FCG rates for A-T samples. Schubbe [4] studied the influence of microstructure orientation on the FCGR for an AA7050-T7451 concluding that, when the rolling direction of microstructure is oriented to the load direction the FCGR decreases. This happens because mixed-mode characteristics of the crack growth lead to a crack redirection, in an intragranular propagation. On the other hand, Wei *et al.* [5] showed that the FCGR increases when the rolling direction of microstructure is oriented perpendicular to the load direction for an AA7050-T7451 due to the presence of less coarsen precipitates at the grain boundary, which allows intergranular propagation.

In order to speed up alloy development process, it is important to understand the links between material microstructural parameters and FCGR [6,7]. It is widely accepted that cyclic plastic deformation at the crack tip is the main damage mechanism behind FCG [2]. Therefore, this study may be done in two steps:

1st link material parameters with cyclic plastic deformation; 2nd link

---

Nomenclature

AA	Aluminum Alloy
C_x, X_{Sat}	Material constants of Lemaître-Chaboche kinematic hardening law
da/dN	Fatigue crack growth rate
E	Young's modulus
P_{max}	Maximum applied force
P_{min}	Minimum applied force
P_{op}	Crack opening force
FCG	Fatigue Crack Growth
FCGR	Fatigue Crack Growth rate
K_{max}	Maximum stress intensity factor
K_{min}	Minimum stress intensity factor
m	Paris law exponent
R	Stress ratio
U*	Crack closure level
ΔK	Stress intensity factor range (K_{max}-K_{min})

|	
$\Delta\varepsilon^p$	Accumulated plastic strain
$\Delta\varepsilon_c^p$	Critical value of accumulated plastic strain
$\bar{\varepsilon}^p$	Equivalent plastic strain
$\dot{\bar{\varepsilon}}^p$	Equivalent plastic strain rate
X	Back stress tensor
Y_0, Y_{sat}, C	Material constants of Swift isotropic hardening law
Σ	Component of the effective Cauchy stress tensor
σ	Deviatoric component of the Cauchy stress tensor
$\acute{X}$	Deviatoric part of the backstress tensor
X_{Sat}	Saturated backstress tensor
$\dot{X}$	Backstress rate
$\dot{\bar{\varepsilon}}^p$	Equivalent plastic strain rate
$d\dot{\varepsilon}^p$	Increment of the plastic strain rate
$\sigma^{Fit}(A)$	Fitted measured values of true stress at data point
σ^{Exp}	Experimentally measured values of true stress at data point
N	Total number of experimental data points
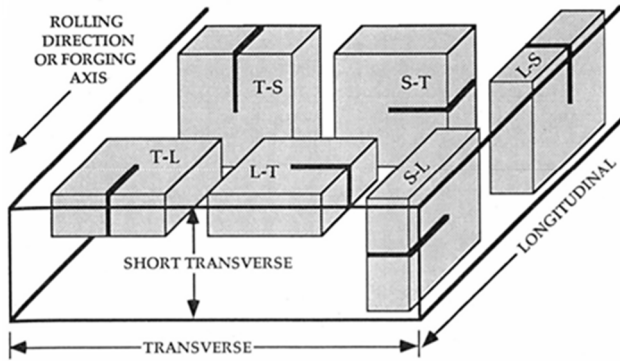
Fig. 1. Orientation of specimens [1].

this deformation with da/dN. In previous works [8,9], the authors used the critical value cumulative plastic deformation at the crack tip, $\Delta\varepsilon_p^c$, as crack driving force. In fact, this parameter quantifies the efficiency of crack tip plastic deformation in producing crack growth. High values of $\Delta\varepsilon_p^c$ indicate that a relatively high cumulative deformation is required to propagate the crack. The values of $\Delta\varepsilon_p^c$ ranged from 261% for the 6082-T6 aluminium alloy (AA) [10] to 78.6% for the 18Ni300 maraging steel [8], being 110% for the AA2024-T351 [8] and 153% for Ti6Al4V obtained by additive manufacturing and submitted to HIP [9].

Therefore, there is a significant influence of the metallic material on the link between cyclic plastic deformation and da/dN, as could be expected. The objective of the present paper is to isolate the effect of material texture in this context, by developing a comparative study of orientations L-T and S-T, illustrated in Fig. 1, using two aluminium alloys. The aluminium alloys studied are the 7050-T7451 and 2050-T8. The series 2xxx and 7xxx are heat-treatable alloys, where the strengthening is achieved mainly by precipitation. The generally accepted precipitation sequence for the high-strength 7000-series aluminium alloys is a supersaturated solid solution → Guinier-Preston zone → metastable

phase η′ → equilibrium phase η ($MgZn_2$). A large number of precipitated phases are randomly distributed inside the grains of the 7050-aluminium alloy [11]. Typical precipitates include the $Al_2Mg_3Zn_3$ phase and rod-like η phase. A dense distribution of small-sized η′ strengthening phases occurs at the crystal boundaries. On the other hand, this work also pretends to show that the AA 2050-T8 is an excellent as a substitute for the AA 7050-T7451 in applications where the components are submitted to cyclic loads.

2. Experimental details

2.1. Material and specimens

The materials studied are the 7050-T7451 and 2050-T8 aluminium alloys, which belong to the heat-treated aluminium alloys series. Table 1 presents the chemical composition, while Table 2 presents the main physical and mechanical properties, made available by the material supplier. The tensile properties listed in Table 2 were obtained only in the L-T direction (see Fig. 1). Both alloys have been widely used in aircraft manufacturing industry due to their good mechanical properties, low density and high corrosion resistance.

Middle-crack tension (M(T)) specimens with 2 mm of thickness were used to study fatigue crack growth. For both aluminium alloys, the specimens were obtained along directions L-T and S-T, as is illustrated in Fig. 1. The extraction of specimens along the thickness (S-T) was only possible due to the large thickness of the original plates. The M(T) samples sizes are presented in Fig. 2 were obtained following ASTM E647 [12] standard. Moreover, tests in strain control for fully-reversed strain ($R_\varepsilon = -1$) were performed according to the procedure described in ASTM E606 standard [13]. These tests were conducted using 8 mm-

Table 2
Physical properties of AA 7050-T7451 and AA 2050-T8. (Constellium company).

AA	Density	Hardness	Ultimate stress	Yield stress
7050-T7451	2.75 g/cm³	185 HV₀.₂	510 MPa	455 MPa
2050-T8	2.7 g/cm³	185 HV₀.₂	524 MPa	460 MPa

Table 1
Chemical composition (wt %) of 7050-T7451 and 2050-T8 aluminium alloys.

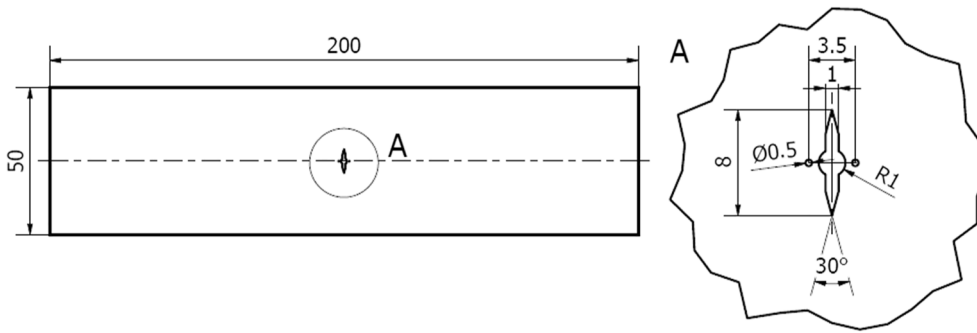| Aluminium alloy	Al	Cu	Cr	Mg	Mn	Ti	Si	Fe	Zn	Li	Ag	Zr
7050-T7451	Bal.	2.17	0.01	2	0.01	0.04	0.04	0.06	6.67	–	–	–
2050-T8	Bal.	3.55	–	0.4	0.35	–	0.04	0.05	0.12	1	0.45	0.1

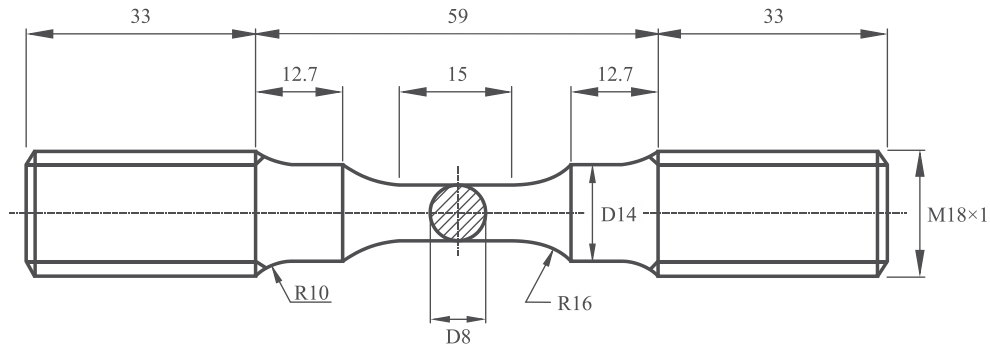**Fig. 2.** Geometry of M(T) samples (dimensions in mm).

Fig. 3. Geometry of specimens for low-cycle fatigue tests (dimensions in mm).
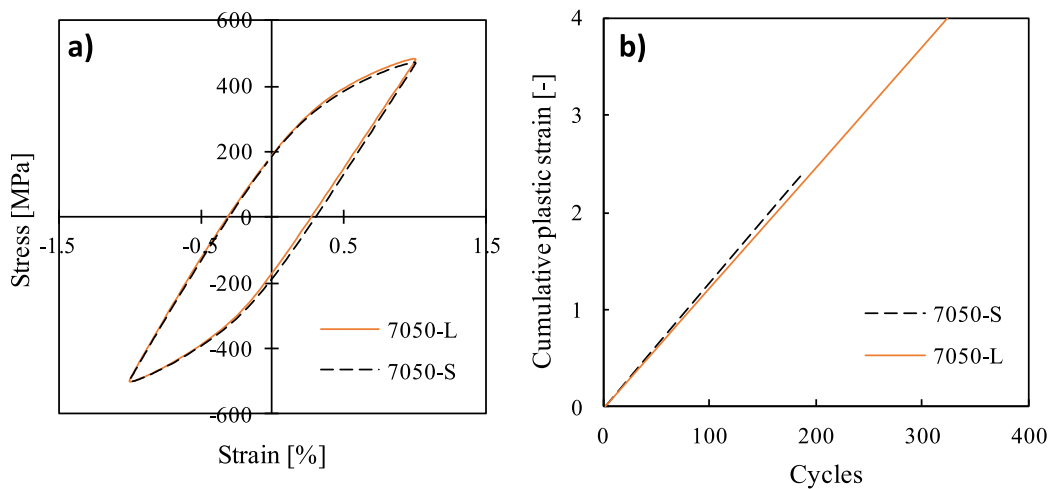

Fig. 4. Effect of specimen orientation on the low-cycle behaviour of the 7050-T7451 aluminium alloy. a) Stress–strain loops. b) Cumulative plastic strain versus number of cycles.

diameter specimens (Fig. 3).

2.2. Low-cycle fatigue testing procedure

Fully-reversed strain amplitude-controlled tests were conducted according to the procedure described in ASTM E606 standard [13], using a computer-controlled 100 kN DARTEC closed-loop servo-hydraulic testing machine, at room temperature, with sinusoidal waves. The total strain amplitude considered was ($\Delta\varepsilon/2$) of $\pm$ 1%, and it was assumed a fixed strain ratio ($R\varepsilon = -1$), and a constant strain rate ($d\varepsilon/dt$) equal to 8 $\times 10^{-3}$ s^{-1}. At least, 200 samples per cycle were collected and recorded using a 12.5 mm-gauge extensometer (model Instron 2620–601) clamped to the specimen *via* two separated knife-edges. The single step test

(SST) was adopted in this research, i.e. each specimen was tested under constant strain amplitude until failure occurs, since the plastic response, in general, is path and history dependent. Tests were interrupted when specimens separated into two pieces.

2.3. Fatigue crack growth testing procedure

Before starting the fatigue crack growth tests, all specimens were polished on one side (according to the ASTM E3-11 [14] standard) for a precise observation of crack tip position. The fatigue tests were performed at the stress ratio R = 0, at room temperature, constant load range, $\Delta P = P_{max}\text{-}P_{min}$, and Mode I loading conditions using a hydraulic testing machine. The crack length, *a*, was obtained by optical
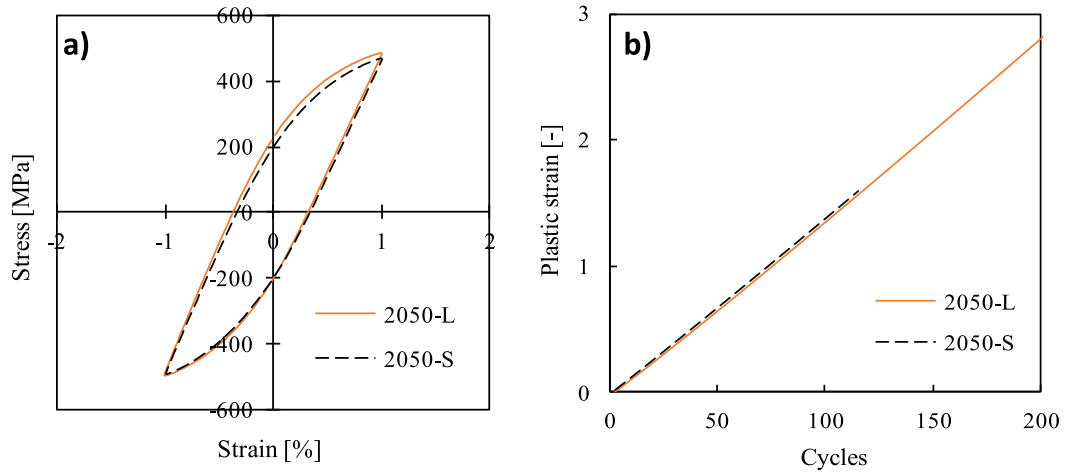
Fig. 5. Effect of specimen orientation on the low-cycle behaviour of the 2050-T8 aluminium alloy. a) Stress–strain loops. b) Cumulative plastic strain versus number of cycles.
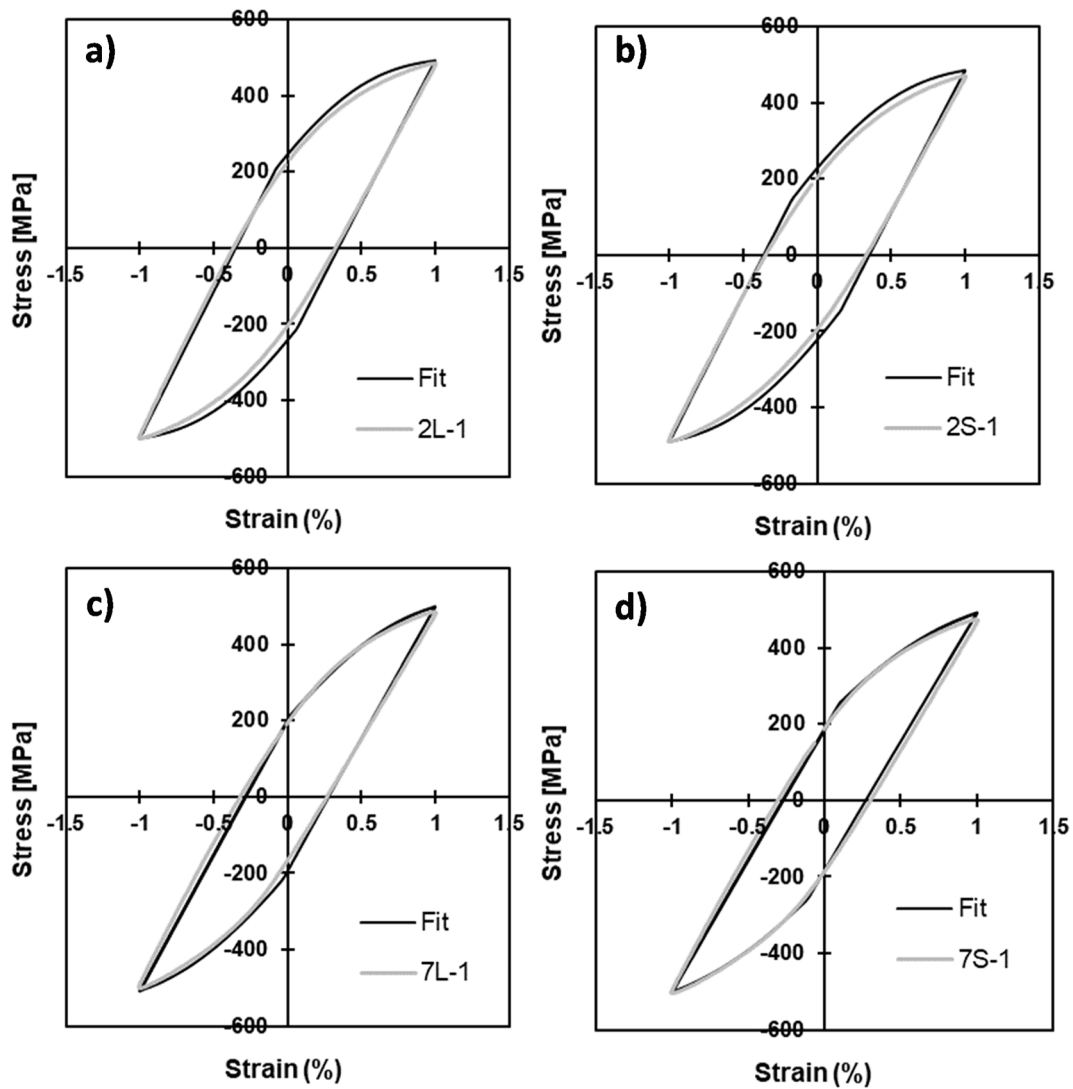

Fig. 6. Comparison between the experimental and fitted half-life cyclic stress–strain curves: a) AA2050-L; b) AA2050-S; c) AA7050-L; d) AA7050-S.

Table 3
Parameters of kinematic hardening for AA2050-T8 and AA7050-T7451.

Material	Y_0 [MPa]	C_X	X_{Sat} [MPa]
2050 L	352.86	462.90	154.58
2050 S	316.87	416.88	188.64
Diff [%]	10.7	10.5	19.8
7050 L	357.93	378.64	183.24
7050 S	375.00	302.47	177.43
Diff [%]	4.7	22.4	3.2

measurement of crack tip position using a travelling microscope (45 ×) attached to a micrometer. The crack growth rates were determined from the *a* versus *N* results, being *N* the number of load cycles, using the secant method proposed in ASTM E647 standard [12]. The results were displayed as *da/dN* vs *ΔK* curves, and the Paris-Erdogan law [15] was fitted to regime II of FCGR for each material and orientation.

Load versus displacement plots were obtained at 1 mm of crack growth for all tests using a pin microgauge extensometer. The gauge pins were placed in two drilled holes of 0.5 mm diameter located above and below the centre of the notch, as is indicated in Fig. 2.

Crack opening load (P_{op}) was quantified using the maximization of the correlation coefficient [16]. It consists in taking the upper 10% of the Load-displacement data and calculating the least squares correlation coefficient. The next data pair is then added, the correlation coefficient is again computed, and this procedure is repeated for the whole data set. The point at which the correlation coefficient reaches a maximum can then be defined as P_{op}. The fraction of load cycle for which the crack remains fully closed is used to quantify the crack closure level:

$$U^* = \frac{P_{op} - P_{min}}{P_{max} - P_{min}} \times 100 \quad (1)$$

2.4. Hardness, metallographic and fracture surface analysis

For a better understanding of the influence of material and orientation on FCGR, hardness profiles, metallographic analysis and fracture surface analysis were made. The two halves of broken samples were prepared and subsequently etched with a solution composed by water (99 ml) and hydrofluoric acid (1 ml), in order to reveal the microstructure of each sample, following the recommendations of ASTM E3-11 [14] standard. After this procedure, the samples were observed and photographed using a Leica DM4000 M LED optical microscope.

The hardness profiles were measured using a Struers Type Duramin microhardness tester along an indentation line at 0.75 mm from crack path and covering the 50 mm of the sample width. The distance between

successive indentations was about 5 mm and a testing load of 200 g was applied for 15 s according to the ASTM E384 [17] standard. Lastly, the fracture surfaces of the broken specimens were analysed with a scanning electron microscope (Philips XL30).

3. Results

3.1. Effect of specimen orientation on plastic deformation

Figs. 4 and 5 presents the cyclic behaviour of the AA7050-T7451 and AA2050-T8, respectively, comparing the L and S orientations. Fig. 4a and 5a plot typical stress–strain loops extracted from intermediate cycles of the low cycle fatigue (LCF) tests (representing about 80% of the total life). The specimen orientation has a minor effect on the cyclic plasticity behaviour of both materials. Comprehensively, Fig. 4b and 5b plot the cumulative plastic strain versus number of load cycles until failure. The linear behaviour indicates that the contribution of each stress–strain loop in terms of plastic strain values remains approximately constant during the tests. Moreover, similar slopes were obtained between lines of L and S orientations, showing that specimen orientation has a minor effect on the cyclic plasticity behaviour of both materials. Nevertheless, for both aluminium alloys, the total number of cycles applied up to fracture is significantly higher in the L orientation, as is highlighted in Fig. 4b and 5b for AA7050-T7451 and AA2050-T8, respectively. Therefore, the macroscopic plastic strain admissible before failure is larger when the material is loaded in the longitudinal (L) orientation.

3.1.1. Fitting of elastic–plastic material parameters

The definition of elastic–plastic material models is an important step in the characterization of cyclic plastic behavior, being of major importance for the development of numerical studies.

The purely kinematic elastic–plastic model adopted in this work assumes: (i) the isotropic elastic behavior modeled by the Hooke's law; (ii) the plastic behavior modelled by the Von Mises yield criterion, coupled with the Armstrong-Frederick non-linear kinematic hardening law under an associated flow rule. The adopted Young modulus is $E = 70$ GPa and $E = 75$ GPa for AA7050-T7451 and AA2050-T8, respectively, while the Poisson ratio is $\nu = 0.3$ for both alloys.

Using the Von Mises formulation where describes the onset of plastic yielding and the Cauchy stress tensor, the Equation (2) can be written as follows:

$$(\Sigma_{22} - \Sigma_{33})^2 + (\Sigma_{33} - \Sigma_{11})^2 + (\Sigma_{11} - \Sigma_{22})^2 + 6(\Sigma_{23}^2 + \Sigma_{13}^2 + \Sigma_{12}^2) = 2Y_0^2 \quad (2)$$

where Σ_{11}, Σ_{22}, Σ_{33}, Σ_{12}, Σ_{13}, and Σ_{23} are the components of the

Fig. 7. Hardness profiles.

Fig. 9. Effect of aluminium alloy on FCGR (R = 0).
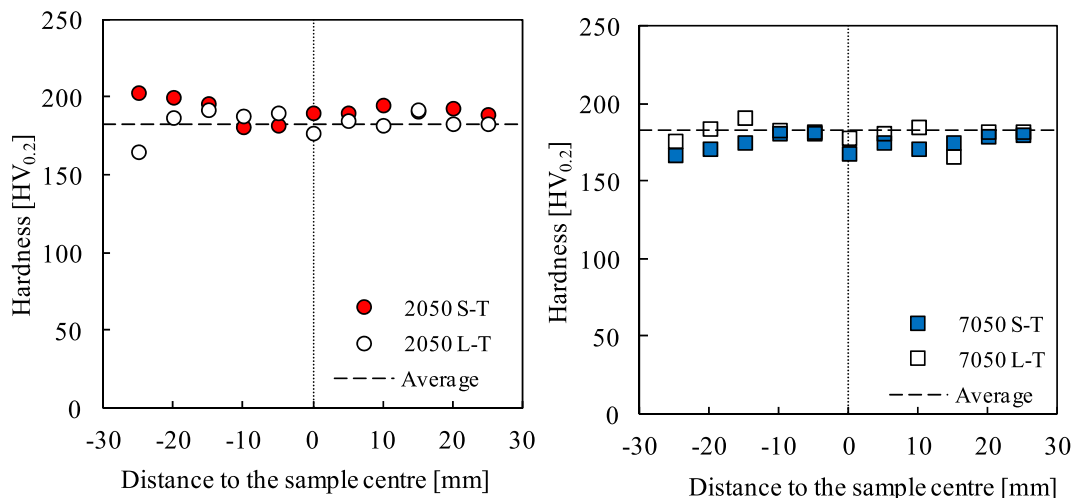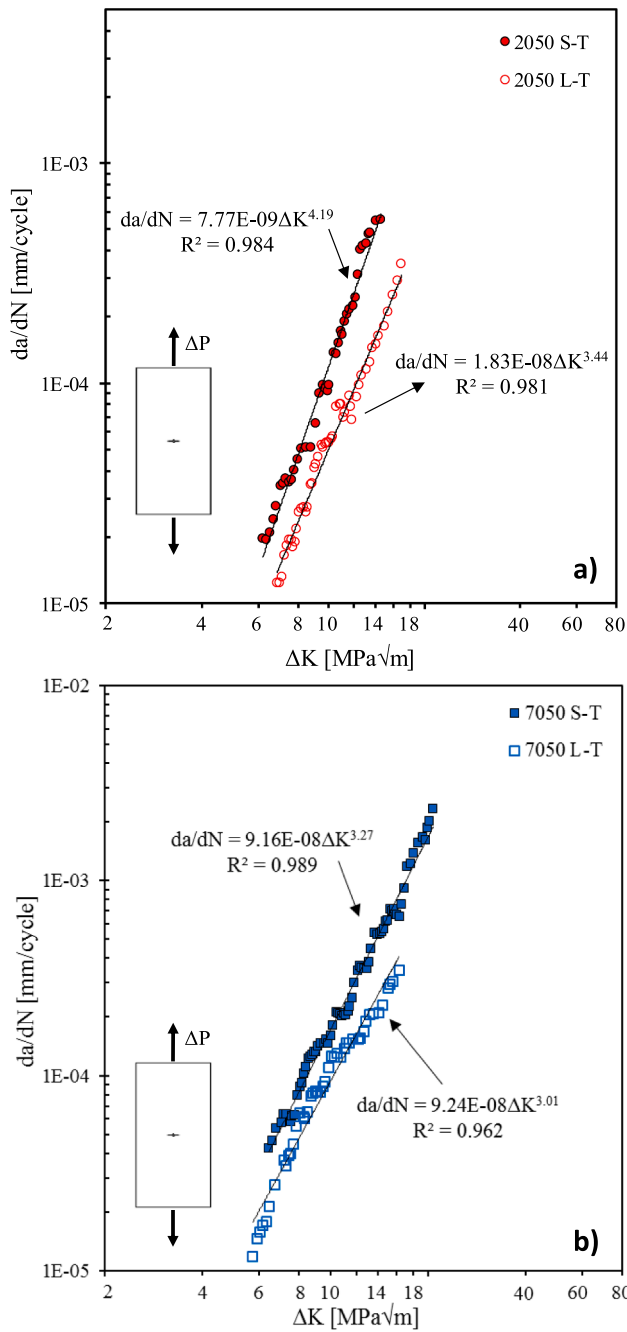
Fig. 8. Effect of specimen orientation on FCGR. a) AA2050-T8. b) AA7050-T7451 (R = 0).

effective Cauchy stress tensor, $\boldsymbol{\Sigma}$ ($\boldsymbol{\Sigma} = \acute{\boldsymbol{\sigma}}\text{-}\acute{\mathbf{X}}$, where $\acute{\boldsymbol{\sigma}}$ and $\acute{\mathbf{X}}$ are the deviatoric components of the Cauchy stress tensor and the deviatoric part of the backstress tensor, respectively), and Y_0 is the initial yield stress; plastic deformation occurs when $\overline{\sigma} = Y_0$, where Y_0 is the initial yield stress. The Armstrong-Frederick law describes the non-linear kinematic hardening as follows [18]:

$$\dot{X} = C_{\mathrm{X}}\left[X_{\mathrm{Sat}}\frac{\Sigma}{\overline{\sigma}} - X^{'}\right]\dot{\overline{\varepsilon}}^{\mathrm{p}} \tag{3}$$

where $\dot{X}$ is the backstress rate, $\overline{\sigma}$ is the equivalent stress, $\dot{\overline{\varepsilon}}^{\mathrm{p}}$ is the equivalent plastic strain rate and C_{X} and X_{Sat} are material parameters. The associated flow rule defines the normality condition, in which the increment of the plastic strain rate, $\mathrm{d}\dot{\varepsilon}^{\mathrm{p}}$, is normal to the yield surface:
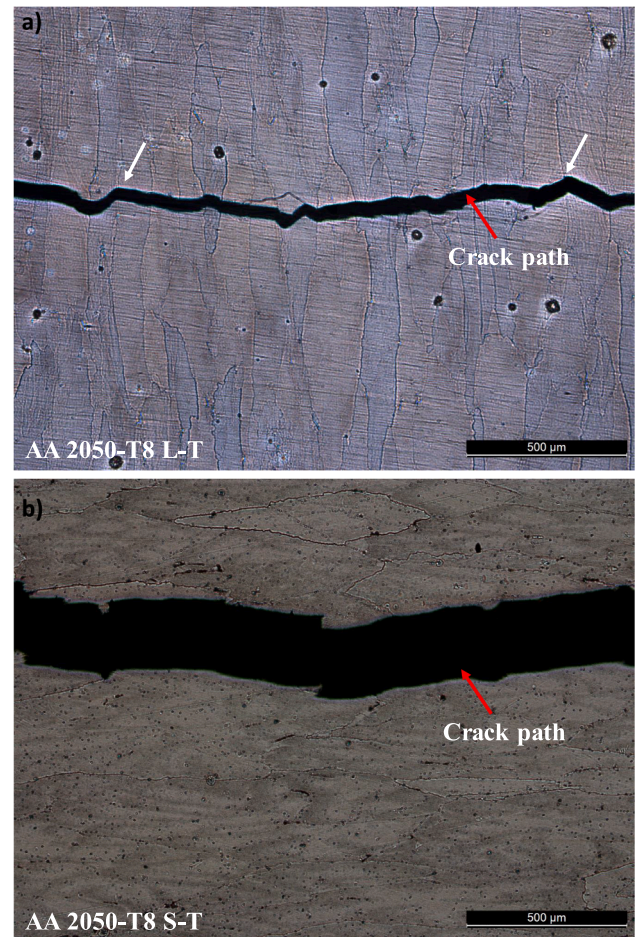

Fig. 10. Effect of specimen orientation on crack path for the AA2025-T8. a) L-T direction. b) S-T direction. (R = 0).
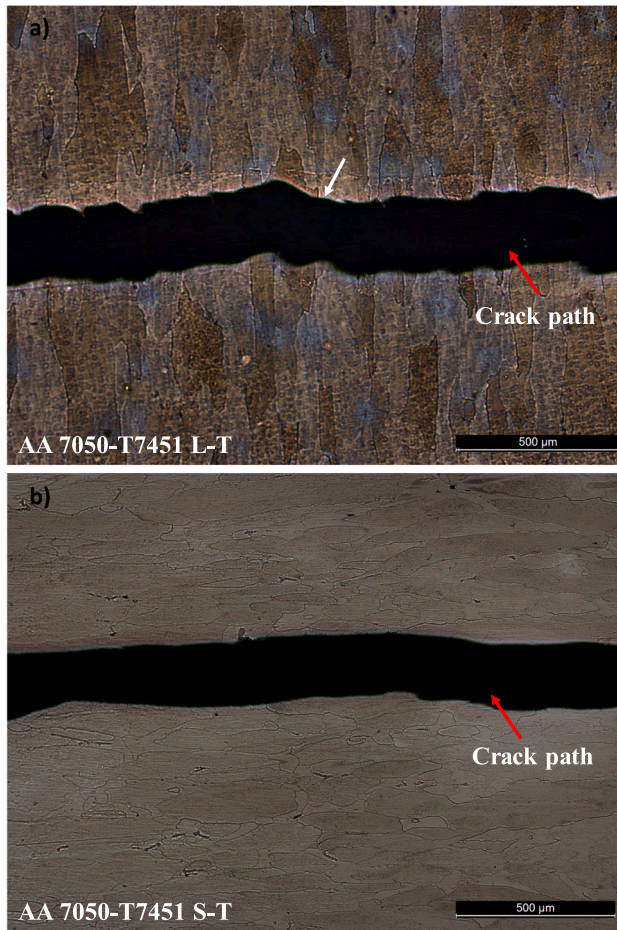
Fig. 11. Effect of specimen orientation on crack path for the AA7050-T7451. a) L-T direction. b) S-T direction (R = 0).

Table 4
U* average values for S-T and L-T directions and both aluminium alloys.

Aluminium alloy	S-T direction U* (average)	L-T direction U* (average)	Variation [%]
AA2050-T8	24.7	32.3	27
AA7050-T7451	22.3	27.8	22

$$\mathrm{d}\dot{\boldsymbol{e}}^{\mathrm{p}} = \dot{\bar{\varepsilon}}^{\mathrm{p}} \frac{\partial\overline{\sigma}(\boldsymbol{\Sigma})}{\partial(\boldsymbol{\Sigma})} \tag{4}$$

The set of material parameters that best describe the cyclic plastic behavior of AA7050-T7451 and AA2050-T8, along the L and S orientations, was determined by an optimization procedure. The set of plastic parameters was obtained by minimization of the least-squares objective function $F(\mathbf{A})$:

$$F(\boldsymbol{A}) = \sum_{i=1}^{N} \left(\frac{\sigma^{\mathrm{Fit}}(\boldsymbol{A}) - \sigma^{\mathrm{Exp}}}{\sigma^{\mathrm{Exp}}} \right)^2_i \tag{5}$$

where $\sigma^{\mathrm{Fit}}(A)$ and σ^{Exp} are, respectively, the fitted and the experimentally measured values of true stress at data point i (which corresponds to a given equivalent plastic strain value); N is the total number of experimental data points, and $\mathbf{A}$ is the set of parameters Y_0, C_X and X_{Sat} to be calibrated. The minimization of $F(\mathbf{A})$ was performed using a non-linear gradient-based optimization algorithm, the GRG2 algorithm [19], included in the Microsoft Excel SOLVER tool. The minimization of the objective function, $F(\mathbf{A})$, was performed for the values of true stress obtained from the half-life cyclic stress–strain curves of both alloys

(AA7050-T7451 and AA2050-T8) and orientations (L and S), which represents about 80% of total life.

Fig. 6 shows the comparison between experimental and numerical stress versus strain results for AA7050-T7451 and AA2050-T8. A good agreement was found between fitted and experimental data of all the studied tests, and therefore the selected fully kinematic hardening model is considered adequate for describing the cyclic behavior of both aluminum alloys. Table 3 lists the identified constants Y_0, C_X and X_{Sat} for both materials and both orientations. For the AA7050-T7451, specimen orientation has a minor effect on Y_0, and X_{Sat}. In a previous study [20] a sensitivity analysis was developed to quantify the relative importance of the different elastic–plastic properties on the FCGR. It was found that Y_0 had a higher effect, followed by X_{Sat} and C_X. Although the higher difference between the identified constants is obtained for the C_X parameter, it is not expected to have a major effect on the FCGR. Therefore, the AA7050-T7451 shows a minor effect of orientation on elastic–plastic model. On the other hand, the AA2050-T8 shows variations of about 10%, which express the small effect of orientation observed in Fig. 5.

3.2. Hardness

Fig. 7 presents the obtained hardness profiles for the two materials and two orientations. As can be seen, there is a small influence of microstructure orientation on the obtained hardness values because all series and aluminium alloys are around the average hardness value of 183 $HV_{0.2}$. In Table 2 a similar value was indicated by the material supplier (185 $HV_{0.2}$). Since the hardness is an indirect measurement of the plastic behaviour of the material, these hardness results confirm the low influence of material orientation on the plastic behaviour.

3.3. Effect of specimen orientation on FCGR

Fig. 8a shows the effect of sample orientation on FCGR results for the AA2050-T8 in regime II. The S-T series curve is above the curve for L-T series, which means that this has a higher resistance to FCGR. A similar trend can be observed in Fig. 8b for the AA7050-T7451, i.e., lower values of FCGR for the L-T orientation. The Paris-law equations are presented in Fig. 8, showing values of m between 3.01 and 4.19, which are typical.

Fig. 9 compares the two aluminium alloys with regard to the L-T direction, which has the best fatigue crack growth performance. The 2050-T8 aluminium alloy shows a better fatigue crack propagation resistance compared with the AA7050-T7451. It is interesting to notice that the influence of orientation, observed in Fig. 8, is as important as the influence of material observed in Fig. 9. These results are according Lequeu *et al.* [21], who concluded that the AA2050 can thus be considered for a direct replacement of parts made of 7050 alloy because it shows a density benefit of about 5%, higher static yield, higher period of fatigue crack initiation and slower crack growth rate.

3.3.1. Crack path

Figs. 10 and 11 present the crack paths obtained for the tested samples. Fig. 10a and 11a show that the crack path for the L-T orientation is perpendicular to the grains, i.e., the propagation is transgranular. When the crack tip finds a grain boundary, as is indicated by the white arrows, it suffers a crack deflection which increases surface roughness. On the other hand, Fig. 10b and 11b, for the S-T orientation, show intergranular crack paths, i.e., the crack propagates along grain boundaries. For this reason, the fracture surfaces are smoother. Therefore, and looking to Fig. 8, the propagation along grain boundaries is easier compared with the propagation through the grain boundaries. Similar trends were observed in the literature, as has already been mentioned in the introduction. Leitner *et al.* [2] showed that, in high purity nickel, cracks propagate easier along the grain boundaries. The presence of grain boundaries perpendicular to the crack growth direction delays crack growth. Leitner *et al.* [3] studied steel with pearlitic
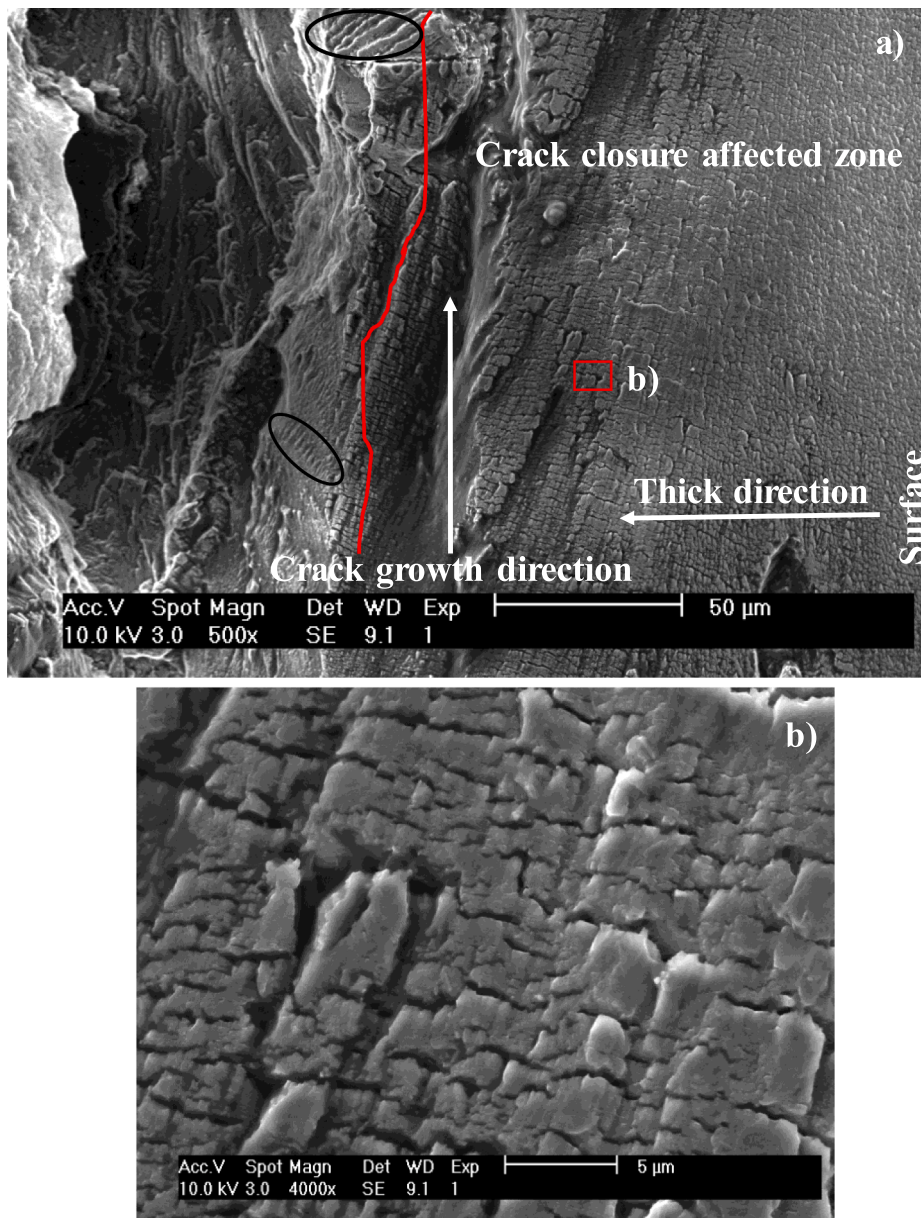
Fig. 12. SEM images of fracture surface for AA 7050-T7451 L-T direction ($\Delta K \approx 12.5$ MPa$\sqrt{m}$).

structure consisting of a lamellar structure of ferrite and cementite. Plastic deformation was used to align the microstructure and reduce lamella spacing. A strong effect of orientation of specimens was found, with lower propagation rates when the crack propagated through the lamellae of the aligned structure, which serve as obstacles. Coarser microstructures were found to reduce the fatigue crack growth rate in the near-threshold regime, and to improve the threshold behaviour for pearlitic steels [22] or cast aluminium alloys [23].

The orientation of the specimens may also have an extrinsic effect linked with crack closure. In fact, the higher roughness observed in Fig. 10a and 11a is expected to increase the crack closure level in regime I and lower part of regime II of FCGR. During the closing process of the fatigue crack, a small mismatch between the matting crack faces can lead a premature contact leading to the crack closure effect. This protective mechanism is more active near threshold and in the lower part of regime II of crack growth, therefore it is not expected to be very relevant in the results presented. Moreover, the crack deflection from mode I reduces FCGR due to two mechanisms [Leitner, 2015]. First, the effective driving force is reduced related to the straight crack. Second, the

true length of a regularly deflected crack is longer than that of a planar crack and, therefore, more cycles are needed to reach a certain macroscopic crack length. Potirniche and Daniewicz [24] simulated crack growth and observed, when the crack-tip reaches the grain boundary, the neighbouring grain orientation exhibited a major influence on the crack opening stress evolution and consequently on the FCGR, whereby a small mismatch in grain orientation facilitates crack growth and vice versa, i.e. a high mismatch angle between both grains reduces the FCGR in the grain boundary region.

3.3.2. Crack closure measurements

Table 4 presents the average values of crack opening level. The U* average values are higher for the L-T direction when compared to the S-T direction in both aluminium alloys, being this effect more pronounced for the AA2050-T8. This behaviour can be used to explain the trends of FCG rates obtained in Figs. 8 and 9. The increase of the crack closure level leads to a decrease of the FCGR since the effective load range is lower. However, an intrinsic effect also exists, associated with the effect of grain boundaries on FCGR. Crack deflection increases surface
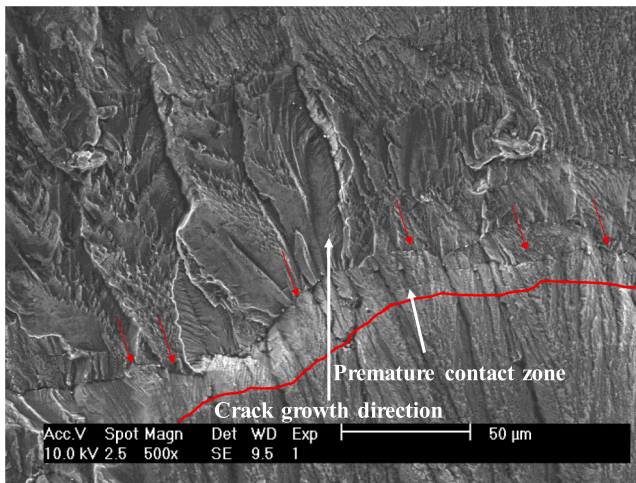
Fig. 13. SEM images of fracture surface for AA 2050-T8 L-T direction ($\Delta K \approx 10.5$ MPa$\sqrt{m}$).

roughness, as is observed in Fig. 10a and 11a, which may produce roughness induced crack closure namely at low load levels. Since the maximum plastic strain attained before failure in LCF is significantly larger in the specimens loaded at the L orientation (Figs. 5 and 6), the cyclic plastic zone would be larger when the M(T) specimen is oriented in the L-T direction. This can lead to an increase of the crack closure level for this direction, as is shown in Table 4.

3.3.3. Fracture surface analysis

Fig. 12a and 12b show an example for AA7050-T7351 L-T of some typical features of the fatigue fracture surfaces for all series. In Fig. 12a can be observed the result in the fracture surface due to the plastic-induced crack closure, more evident close to the surface (on right-hand side) where are submitted to plane stress state. The material in this zone suffered a higher plasticity due to the crack growth causing a premature contact thereby inducing crack closure being higher in the L-T samples. Fig. 12b shows high magnification of this zone where is possible to see a smooth surface due to the premature contact and highly deformed by the plastic wedge induced in the crack growth. In Fig. 12a, is a poor defined crack growth striation (marked by black balloons) can be observed that evidences the transgranular fatigue propagation. The higher crack closure values registered in the L-T series were attributed to the crack deflection.

In the Fig. 13 are presented an example of this phenomena for the AA 2050-T8 S-T series is shown. Marked by red arrows can be observed the crack deflection and the premature contact zone (marked by a red line). The crack deflexion zone presents a deviation of $\pm$ 45° from the linear crack path.

4. Discussion

Cyclic plastic deformation is assumed to be the main driving mechanism of FCG. This ductile fracture mechanism makes the crack propagate both along the grain boundaries and through these boundaries. However, the movement of dislocations is not exactly the same in each situation. For both aluminium alloys studied, the FCGR is lower in the L-T orientation (Fig. 8). This is related with both shape and orientation of the grains in the specimen, i.e. material anisotropy, which is consequence of the rolling process. Since the elongated grains are aligned with the loading direction for the L-T specimen orientation (Fig. 10a and Fig. 11a), the crack propagation is transgranular. On the other hand, for the S-T orientation the crack propagates along grain boundaries since the grains are aligned with the crack front (Fig. 10b and Fig. 11b). Therefore, the FCGR is larger in the S-T orientation because the grain

boundaries are preferential crack paths.

Although the cyclic plastic behaviour of both alloys is identical in terms of stress–strain loops (Fig. 4a and Fig. 5a), the number of loading cycles required to achieve fracture in low cycle fatigue tests is significantly larger in the L orientation (Fig. 4b and Fig. 5b). Hence, the material anisotropy can affect low cycle fatigue tests, namely the number of load cycles until failure. Since the contribution of each stress–strain loop in terms of plastic strain rise is identical for both directions, the maximum plastic strain admissible before failure is larger in the longitudinal direction. Therefore, FCGR is lower when the loading occurs in the longitudinal direction, i.e. in the L-T specimen orientation.

For both aluminium alloys, the low cycle fatigue tests show that the admissible total plastic strain before failure is larger when the specimen is loaded in longitudinal direction. Accordingly, larger values of plastic deformation are expected at the crack tip in the L-T specimen orientation. This induces a larger residual plastic wake and consequently increases the crack closure level (Table 4) due to the plastic-induced crack closure.

The impact of the specimen orientation on the crack growth rate can be also related to the distribution of the plastic deformation. The stress and plastic deformation are uniform in low cycle fatigue tests, while the stress and strain field are complex around the crack tip. The locality of the plastic deformation in the CT specimens enlarges the importance of the microstructure in comparison with the low cycle fatigue results. Thus, the impact of the material microstructure is higher in the fatigue crack growth analysis than in the stress–strain loops from the LCF tests. In the present numerical approach, this local effect is accounted for using the critical cumulative plastic strain.

5. Conclusions

The main objective here was the experimental study of the effect of microstructure orientation on fatigue crack growth (FCGR). This research was made using M(T) specimens with 2 mm thick made of 7050-T7451 and 2050-T8 aluminium alloys. The orientations considered related to crack propagation direction were the L-T and S-T. Two main aspects were considered: the effect on orientation of cyclic plastic deformation, which is widely accepted to be the main failure mechanism, and the effect of orientation on FCGR. The main conclusions are:

● There is a limited effect of orientation on the cyclic plastic behaviour of the two aluminium alloys. This was studied using low-cycle fatigue specimens and hardness measurements. The mathematical modelling of the elastic–plastic behaviour reflects this independence related to orientation. Nevertheless, the number of loading cycles required to achieve fracture in low cycle fatigue is significantly larger when the grains are aligned with the loading direction (L orientation).
● The fatigue crack growth rate is lower when the grains are aligned to the load direction (L-T samples), which agrees with the results from the low cycle fatigue tests. In this case the crack propagation is transgranular. Thus, the plastic strain allowable at crack tip is larger in the L-T specimen orientation. This induces a larger residual plastic wake and consequently increases the crack closure. The AA2050-T8 showed a better fatigue crack propagation performance presenting a higher crack closure value.

Declaration of Competing Interest

The authors declare that they have no known competing financial interests or personal relationships that could have appeared to influence the work reported in this paper.

References

[1] Anderson TL. Fracture Mechanics: Fundamentals and Applications. 4th Ed. CRC Press; 2017.

[2] Leitner T, Hohenwarter A, Pippan R. Revisiting fatigue crack growth in various grain size regimes of Ni. Mater Sci Eng A 2015;646:294–305. https://doi.org/10.1016/j.msea.2015.08.071.

[3] Leitner T, Trummer G, Pippan R, Hohenwarter A. Influence of severe plastic deformation and specimen orientation on the fatigue crack propagation behavior of a pearlitic steel. Mater Sci Eng, A 2018;710:260–70.

[4] Schubbe JJ. Fatigue crack propagation in 7050–T7451 plate alloy. Eng Fract Mech 2009;76(8):1037–48.

[5] Wei L, Pan Q, Huang H, Feng L, Wang Y. Influence of grain structure and crystallographic orientation on fatigue crack propagation behavior of 7050 alloy thick plate. Int J Fatigue 2014;66:55–64.

[6] Carpinteri A, Spagnoli A. A fractal analysis of size on fatigue crack growth. Int J Fatigue 2004;26(2):125–33.

[7] Carpinteri A, Spagnoli A, Vantadori S. A multifractal analysis of fatigue crack growth and its application to concrete. Eng Fract Mech 2010;77(6):974–84.

[8] Borges MF, Neto DM, Antunes FV. Numerical simulation of fatigue crack growth based on accumulated plastic strain. Theor Appl Fract Mech 2020;108:102676. https://doi.org/10.1016/j.tafmec.2020.102676.

[9] Ferreira FF, Neto DM, Jesus JS, Prates PA, Antunes FV. Numerical Prediction of the Fatigue Crack Growth Rate in SLM Ti-6Al-4V Based on Crack Tip Plastic Strain. Metals 2020;10(9):1133. https://doi.org/10.3390/met10091133.

[10] JPF Pais, Propagação de Fendas por Fadiga: Comparação Entre Resultados Numéricos e Experimentais, Master Thesis, University of Coimbra, November 2021.

[11] Branco R, Costa JD, Borrego LP, Wu SC, Long XY, Zhang FC. Effect of strain ratio on cyclic deformation behaviour of 7050–T6 aluminium alloy. Int J Fatigue 2019;129:105234. https://doi.org/10.1016/j.ijfatigue.2019.105234.

[12] ASTM. Standard test method for measurement of fatigue crack growth rates. Annual Book of ASTM Standards Volume 03.01, ASTM E 647, 2000.

[13] ASTM E606/E606M, 2019 standard test method for strain controlled fatigue testing.

[14] ASTM Standard E3, 2011. Standard Guide for Preparation of Metallographic Specimens. ASTM 386 International, West Conshohocken, PA, 2011, DOI: 10.1520/E0003-11, www.astm.org.

[15] Paris P, Erdogan F. A Critical Analysis of Crack Propagation Laws. J Basic Eng 1963;85(4):528.

[16] Allison JE, Ku RC, Pompetzki MA. A comparison of measurement methods and numerical procedures for the experimental characterization of fatigue crack closure. In: Newman JC, Elber W, editors. Mechanics of fatigue crack closure, ASTM STP 982. Philadelphia: American Society for Testing and Materials; 1988. p. 171–85.

[17] ASTM Standard E384, 2011e1. Standard Test Method for Knoop and Vickers Hardness of Materials. ASTM 388 International, West Conshohocken, PA, 2011, DOI: 10.1520/E0384-11E01, www.astm.org.

[18] Chaboche JL. A review of some plasticity and viscoplasticity constitutive theories. Int J Plast 2008;24:1642–93.

[19] Lasdon LS, Waren AD, Jain A, Ratner MW. Design and testing of a Generalized Reduced Gradient Code for Nonlinear Optimization. Cleveland: NTIS National Technical Information Service U. S. Department of Commerce; 1975.

[20] Borges MF, Antunes FV, Prates PA, Branco R, Vojtek T. Effect of Young's modulus on Fatigue Crack Growth. Int J Fatigue 2019;132:105375.

[21] Lequeu Ph, Smith KP, Daniélou A. Aluminum-Copper-Lithium Alloy 2050 Developed for Medium to Thick Plate. J Mater Eng Perform 2010;19(6):841–7.

[22] Gray GT, Williams JC, Thompson AW. Roughness-Induced Crack Closure: An Explanation for Microstructurally Sensitive Fatigue Crack Growth. Metall Trans A 1983;14(2):421–33. https://doi.org/10.1007/BF02644220.

[23] Lados DA, Apelian D, Donald JK. Fatigue crack growth mechanisms at the microstructure scale in Al–Si–Mg cast alloys: Mechanisms in the near-threshold regime. Acta Mater 2006;54(6):1475–86. https://doi.org/10.1016/j.actamat.2005.11.019.

[24] Potirniche GP, Daniewicz SR. Finite element modeling of microstructurally small cracks using single crystal plasticity. Int J Fatigue 2003;25(9):877–84. https://doi.org/10.1016/S0142-1123(03)00124-5.